

# Focusing light inside scattering media with magnetic-particle-guided wavefront shaping

HAOWEN RUAN,<sup>1,\*</sup> TOM HABER,<sup>2</sup> YAN LIU,<sup>1</sup> JOSHUA BRAKE,<sup>1</sup> JINHO KIM,<sup>1</sup> JACOB M. BERLIN,<sup>2</sup> AND CHANGHUEI YANG<sup>1</sup>

<sup>1</sup>Department of Electrical Engineering, California Institute of Technology, Pasadena, California 91125, USA

<sup>2</sup>Department of Molecular Medicine, Beckman Research Institute at City of Hope, Duarte, California 91010, USA

\*Corresponding author: hruan@caltech.edu

Received 21 August 2017; revised 27 September 2017; accepted 28 September 2017 (Doc. ID 305214); published 25 October 2017

Optical scattering has traditionally limited the ability to focus light inside scattering media such as biological tissue. Recently developed wavefront shaping techniques promise to overcome this limit by tailoring an optical wavefront to constructively interfere at a target location deep inside scattering media. To find such a wavefront solution, a “guide-star” mechanism is required to identify the target location. However, developing guidestars of practical usefulness is challenging, especially in biological tissue, which hinders the translation of wavefront shaping techniques. Here, we demonstrate a guidestar mechanism that relies on magnetic modulation of small particles. This guidestar method features an optical modulation efficiency of 29% and enables micrometer-scale focusing inside biological tissue with a peak intensity-to-background ratio (PBR) of 140; both numbers are one order of magnitude higher than those achieved with the ultrasound guidestar, a popular guidestar method. We also demonstrate that light can be focused on cells labeled with magnetic particles, and to different target locations by magnetically controlling the position of a particle. Since magnetic fields have a large penetration depth even through bone structures like the skull, this optical focusing method holds great promise for deep-tissue applications such as optogenetic modulation of neurons, targeted light-based therapy, and imaging. © 2017 Optical Society of America

**OCIS codes:** (190.5040) Phase conjugation; (110.0113) Imaging through turbid media; (110.1080) Active or adaptive optics; (090.2880) Holographic interferometry.

<https://doi.org/10.1364/OPTICA.4.001337>

## 1. INTRODUCTION

The ability to focus light deep inside scattering media such as biological tissue is critical to many applications, such as high-resolution optical imaging, noninvasive optogenetics, light-based therapy, microsurgery, and optical tweezing. However, the strong optical scattering inherent to many types of biological tissue prevents conventional optics from focusing light beyond depths of  $\sim 1$  mm, since at this depth nearly all the light has been scattered [1]. To break this optical diffusion limit, wavefront shaping techniques [2–6] are being actively developed to harness the multiply scattered light. These techniques control the optical field on a target plane inside a scattering medium by shaping the optical field on an input plane outside the medium. The relationship between the input plane and target plane can be described by a transmission matrix, which characterizes the propagation of light through the scattering medium [7,8].

To gain control over the optical field on the target plane, one needs to measure the transmission matrix. While extensive transmission matrix measurement enables control over a large area on the target plane [9,10], measuring a small part of the transmission matrix is preferable for applications involving highly dynamic

samples like living tissue due to the problem of tissue decorrelation [11–14]. A good example is focusing light to a spot inside a scattering sample, in which case one needs to measure only a single row of the transmission matrix [5]. In this instance, one can use either a feedback-based approach to optimize the light intensity at a spot inside the sample [3] or digital optical phase conjugation (DOPC) to directly measure the light field from an embedded point source [15–20]. The latter has an advantage in operation speed as it enables light field measurement in parallel using sensor arrays and therefore shows promise for applications involving dynamic samples.

No matter which method is used to measure the transmission matrix, accessing the target plane is necessary. In practice, however, the target plane inside a scattering medium is often not directly accessible, especially when minimally invasive approaches are desired. To address this problem, previous approaches resort to indirect access to the target plane by designing a “guidestar” mechanism [5].

Until now, only a few guidestar mechanisms have been reported. These guidestars can be loosely categorized based on their controlling mechanisms. The first category is using light itself to control the guidestar, and includes fluorescence [21,22],

second-harmonic generation [16], absorption [9,23–25], and coherence gating [26]. However, fluorescence has low coherence and second-harmonic generation is generally inefficient, limiting their working depth with DOPC. Because optical absorption alone cannot generate light for phase conjugation and coherence gating is limited to shallow depths, these approaches are not suitable for DOPC either and have not been used as guidestars for DOPC thus far. The second category employs ultrasound and includes ultrasound [27–31] and ultrasound microbubble guidestars [32]. Although ultrasound offers excellent localization, it also introduces intrinsic drawbacks such as a large focal volume, low modulation efficiency, lack of biomolecule specificity, strong attenuation at high frequency, low penetration through some structures like bones or gas, and the need for coupling agents. Although ultrasound microbubbles address the first three problems of the ultrasound guidestar, they are largely limited to applications in the vasculature. The third type of guidestar mechanism does not rely on any external driving fields. Instead, it utilizes the intrinsic motion of an object such as a flowing red blood cell [33,34], which largely limits its biomedical applications to the vasculature. Moreover, one cannot freely control the location of the focus.

Here, we report a new category of guidestar, which uses a magnetic field as the controlling mechanism. Compared with light and sound fields, the magnetic field has excellent penetration depth, and thus the achievable focusing depth of this guidestar is no longer limited by the attenuation of the controlling fields. Similarly to light and sound fields, the magnetic field has been used extensively in biomedical diagnosis and research. A prominent example is magnetic resonance imaging (MRI), which is

widely used for full-body human imaging. Coupled with magnetic particles, magnetic fields have also been used for applications such as biomolecule and cell separation [35], cell migration control [36], hyperthermia-based therapy and controlled drug delivery [37], and magnetothermal neural stimulation [38]. Here we use magnetic-field-driven magnetic particles as a new guidestar mechanism. As a proof-of-concept demonstration, we first focus light onto a magnetic particle sandwiched between two pieces of scattering tissue. We then demonstrate that we can also focus light to a targeted cell that has endocytosed magnetic particles. Furthermore, by controlling the position of the particle using an external magnetic field, we demonstrate light focusing to different targeted locations between two pieces of scattering tissue.

## 2. METHODS

The basic operation of the magnetic particle guidestar is illustrated in Fig. 1 (see Fig. S1 of Supplement 1 for a detailed setup). As light travels into the biological tissue, its beam size is broadened in space due to multiple scattering [Fig. 1(a)]. As it passes through the tissue, part of the scattered light interacts with the magnetic particles embedded deep inside the tissue. If the DOPC system can selectively detect light that interacts with the magnetic particles, the magnetic particle is effectively a light source or a guidestar embedded inside the tissue [5]. Once the DOPC system measures the light field from the guidestar, it can reconstruct a phase-conjugated copy, which retraces the scattering trajectories back to the location of the guidestar, based on the principle of optical phase conjugation [39,40] [Fig. 1(b)]. We

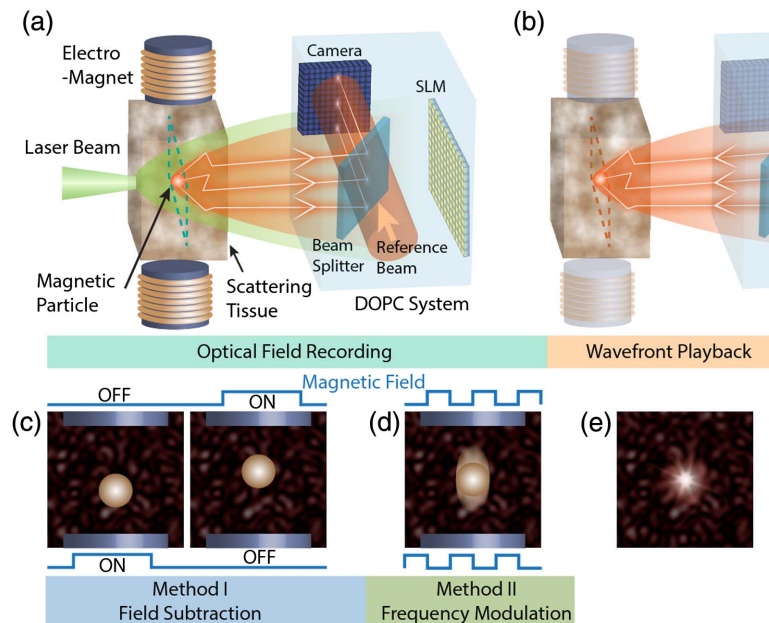


**Fig. 1.** Principle of magnetic-particle-guided optical focusing. (a) A magnetic particle is embedded in a piece of scattering tissue. A portion of the impinging laser beam interacts with the particle and the resulting tagged light is detected interferometrically using the camera of a DOPC system. (b) After capturing the field of the tagged light, the conjugate wavefront is displayed on the spatial light modulator (SLM) of the DOPC system. The reconstructed conjugate light field then retraces the scattering paths and forms a focus at the location of the magnetic particle. Panels (c) and (d) show two methods to separate the tagged light field from the background unmodulated light. The field subtraction method in (c) captures two optical fields before and after a magnetic field displaces the magnetic particle. The differential field nullifies the contribution from the background, which is not scattered by the particle. The frequency modulation method shown in (d) uses an AC magnetic field to make the magnetic particle oscillate, which shifts the frequency of the light, which interacts with the particle. By matching the frequency of a planar reference beam with that of the tagged light, the DOPC system detects the tagged light field via phase-shifting holography. (e) After imprinting the conjugate wavefront of the tagged light on a planar reference beam using the SLM, the conjugate wave forms a bright focus on top of a dim background at the location of the magnetic particle inside the scattering medium.

developed two methods to allow the DOPC system to selectively detect the light that interacts with the magnetic particles.

### A. Field Subtraction Method

The first method is called “field subtraction” and is conceptually similar to the kinetic guidestar [33,34]. In this method, we used a magnetic field to displace the magnetic particle, which alters the optical field that interacts with the magnetic particle [Fig. 1(c)]. By taking the difference between the two optical fields measured before and after displacing the magnetic particle, we were able to measure the optical field modulated by the particle displacement. Mathematically, the first optical field on the target plane,  $E_{t_1}(x, y)$ , can be decomposed into a background field  $E_b(x, y)$ , which does not interact with the particle and a modulated field  $E_{m_1}(x, y)$ , which interacts with the particle, yielding  $E_{t_1}(x, y) = E_b(x, y) + E_{m_1}(x, y)$ . Since we use DOPC, it is more convenient to discretize the functions into column vectors (i.e.,  $\mathbf{E}_{t_1} = \mathbf{E}_b + \mathbf{E}_{m_1}$ ), each of which contains  $n$  complex elements. In this representation, each element in the column vector maps to an optical mode on the two-dimensional target plane. Similarly, we can describe the second field as  $\mathbf{E}_{t_2} = \mathbf{E}_b + \mathbf{E}_{m_2}$ , where  $\mathbf{E}_{t_2}$  is the field at the target plane and  $\mathbf{E}_{m_2}$  is the field that interacts with the particle after it was displaced by the external magnetic field. The light fields measured on the camera plane (or input plane) can be connected to the optical fields on the target plane through a transmission matrix  $\mathbf{T}$  such that  $\mathbf{E}_1 = \mathbf{T}\mathbf{E}_{t_1} = \mathbf{T}(\mathbf{E}_b + \mathbf{E}_{m_1})$  and  $\mathbf{E}_2 = \mathbf{T}\mathbf{E}_{t_2} = \mathbf{T}(\mathbf{E}_b + \mathbf{E}_{m_2})$ . Here,  $\mathbf{T}$  is an  $m \times n$  matrix whose elements follow a circular Gaussian distribution and  $\mathbf{E}_1$  and  $\mathbf{E}_2$  are column vectors of  $m$  elements, where each element represents an optical mode on the camera plane before and after particle displacement, respectively. Taking the difference between these two measured fields, we have  $\Delta\mathbf{E} = \mathbf{E}_2 - \mathbf{E}_1 = \mathbf{T}(\mathbf{E}_{m_2} - \mathbf{E}_{m_1})$ . Here, the field subtraction effectively removes the background field on the measurement plane, resulting in a field that describes the modulation by the magnetic guidestar. Finally, we playback the conjugated differential field  $\Delta\mathbf{E}^*$  with an optical gain  $\alpha$  provided by the playback beam (where  $*$  denotes a conjugate transpose). Assuming time-reversal symmetry, we can calculate the resulting playback field  $\mathbf{E}_p$  on the target plane by multiplying  $\mathbf{T}$  from the left with  $\Delta\mathbf{E}^*$ :

$$\begin{aligned} \mathbf{E}_p &= \alpha\Delta\mathbf{E}^*\mathbf{T} \\ &= \alpha[(\mathbf{E}_{m_2}^* - \mathbf{E}_{m_1}^*)\mathbf{T}^*]\mathbf{T} \\ &= \alpha\beta(\mathbf{E}_{m_2}^* - \mathbf{E}_{m_1}^*). \end{aligned} \quad (1)$$

Here we assume minimal absorption within the sample to apply the approximation  $\mathbf{T}^*\mathbf{T} \approx \beta\mathbf{I}$ , where  $\beta$  is the fraction of scattered light that is measured by the DOPC system and  $\mathbf{I}$  is an identity matrix. The playback light effectively cancels out the random transmission matrix to refocus at the locations of the magnetic particle.

In our experiment, we moved the magnetic particles by changing the direction of the magnetic field and the field gradient using a pair of electromagnets [Fig. 1(c) and Fig. S1 of Supplement 1], and captured the light fields exiting the scattering media before and after particle displacement using four-step phase-shifting holography [41]. Then, by subtracting these two measured fields, the background light field not diffracted by the particles is canceled, and we can obtain the field of the tagged light.

### B. Frequency Modulation Method

The second method to measure the wavefront of the light tagged by the magnetic particle is called “frequency modulation.” In this method, we generated an AC magnetic field, which produced a time-varying magnetic field gradient to oscillate the magnetic particles [Fig. 1(d)]. Since the magnetic particles contain iron oxide, which has strong absorption at the 532 nm wavelength of the laser (absorption coefficient  $\sim 10^5 \text{ cm}^{-1}$  [42]), the motions of the particles mainly modulate the amplitude of the light that interacts with them. Based on this assumption, the optical field of the modulated light, as a function of time, can be expressed as

$$E_m(t) = f(t)A \exp[-i(2\pi f_0 t + \varphi_0)], \quad (2)$$

where  $f_0$  is the laser frequency;  $A$  and  $\varphi_0$  are, respectively, the amplitude and phase of the light; and  $f(t)$  is a rectangular modulation function with a fundamental frequency of  $f_m$ , pulse duration of  $\tau$ , and an initial phase of  $\varphi_m$ . To analyze the spectral composition of  $f(t)$ , we expand it into a Fourier series:

$$\begin{aligned} f(t) &= \sum_{n=1}^{\infty} \frac{\sin(\pi n \tau f_m)}{n\pi} \\ &\times \{ \exp[-i(2\pi n f_m t + \varphi_m)] + \exp[i(2\pi n f_m t + \varphi_m)] \} + \tau f_m. \end{aligned} \quad (3)$$

By substituting  $f(t)$  into  $E_m(t)$  in Eq. (2), we obtain

$$\begin{aligned} E_m(t) &= \sum_{n=1}^{\infty} \frac{A}{n\pi} \sin(\pi n \tau f_m) \exp\{-i[2\pi(f_0 + n f_m)t + \varphi_0 + \varphi_m]\} \\ &+ \sum_{n=1}^{\infty} \frac{A}{n\pi} \sin(\pi n \tau f_m) \exp\{-i[2\pi(f_0 - n f_m)t + \varphi_0 - \varphi_m]\} \\ &+ \tau f_m A \exp[-i(2\pi f_0 t + \varphi_0)]. \end{aligned} \quad (4)$$

From Eq. (4), we can see that the frequency of the portion of the light field that interacted with the particle is shifted by  $\pm n f_m$ . It should be noted that in practice the modulation mechanisms also include phase modulation, since the particle motion also alters the optical path length. In this case, the phase modulation also generates harmonic side bands. Therefore, to measure the wavefront of the tagged light out of the background (whose frequency is  $f_0$ ), we can simply tune the frequency of the reference beam to one of the frequencies of the tagged light and perform four-step phase-shifting holography [41,43]. Then, using the spatial light modulator (SLM) inside the DOPC system, we can generate the phase conjugate light field, which will focus to the location of the magnetic guidestar deep inside the scattering medium [Fig. 1(e)].

## 3. RESULTS

### A. Focusing Light inside Scattering Media Using Magnetic-Particle-Guided Optical Phase Conjugation

To demonstrate magnetic-particle-guided optical focusing, we modified the system shown in Figs. 1(a) and 1(b) to enable direct observation of the light intensity at the target plane [Figs. 2(a) and 2(b), respectively]. In this case, the magnetic particles (2.5  $\mu\text{m}$  mean diameter; see Fig. S2 of Supplement 1 for particle characterization) were placed in a microfluidic channel, which was embedded between two pieces of 1-mm-thick chicken breast tissue (see Supplement 1 for sample preparation). The tissue on the observation system side [left side as shown in Fig. 2(a) and 2(b)]

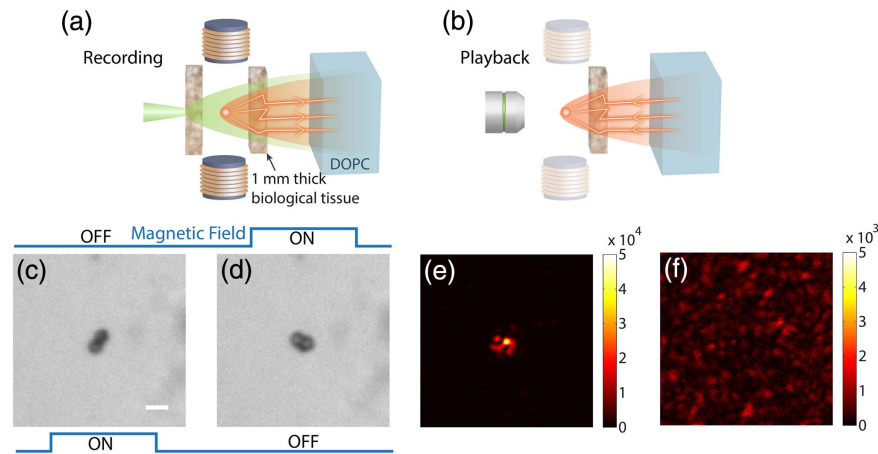


**Fig. 2.** Magnetic-particle-guided optical focusing with the field subtraction method. (a) Schematic of the setup to record the field of the tagged light. (b) Schematic of the setup for playback of the tagged field and observation of the focus. In this step, the tissue on the left side was removed and an imaging system was used to observe the light intensity distribution on the magnetic particle plane. Panels (c) and (d) show bright-field images of the particles with the magnetic field in different directions. (e) The focus observed with the setup shown in (b). (f) Control experiment: no focus was observed when the magnetic fields were turned off and the experiment was repeated. Scale bar, 5  $\mu\text{m}$ .

can be translated in and out of the system to allow the magnetic particles and light intensity to be observed directly using an imaging system [Fig. 2(b); see also Fig. S1 of Supplement 1 for a detailed setup].

We first demonstrated optical focusing through the scattering medium using the field subtraction method. To observe particle displacement due to switching of the external magnetic field, we directly imaged the magnetic particles as shown in Fig. 2(c) and 2(d). The measured displacement of the particles was 1.7  $\mu\text{m}$ . We then put the tissue back in place [Fig. 2(a)] and implemented the field subtraction method to measure and compute the playback light field. A strong focus can be directly observed through the imaging system [Fig. 2(b) and 2(e)]. As a control, we turned off both magnetic fields and repeated the experiment, and no observable focus was created [Fig. 2(f)].

We quantified the focus created by using the field subtraction method. Here, we selected a column across the pixel of maximum intensity out of the image [Fig. 2(e)] and fitted this column with a Gaussian profile. We then took the amplitude of the Gaussian profile as the peak intensity. To calculate the background intensity, we shifted the pattern on the SLM by 10 pixels in both directions to break the phase conjugation relationship, resulting in a background image. The background intensity was then calculated by taking the mean intensity of this image. The PBR of the focus shown in Fig. 2(e) is  $140 \pm 4$ , which is one to two orders of magnitude higher than those achieved with the ultrasound guidestar [28,29]. The full width at half-maximum (FWHM) of the focus, which is defined as the FWHM of the fitted Gaussian profile, is  $1.24 \pm 0.04 \mu\text{m}$ , which is  $\sim 25$  times smaller than the size of the ultrasound guidestar. The error estimation is based on the 95% confidence bounds of the fitting. The magnetic guidestar has a similar performance in terms of both PBR and resolution compared to the ultrasound microbubble guidestar, because both methods involve the use of micrometer-scale physical guidestars.

We also demonstrated optical focusing with the frequency modulation method using the same setup. Here, we drove two electromagnets with 25 Hz rectangular waves ( $f_m = 25 \text{ Hz}$ , duty cycle = 40%, power = 6 W) with a phase shift of  $\pi$  be-

tween the two signals (see Visualization 1 and Visualization 2 for particle motion). To measure the magnetic-guidestar-tagged light, we also shifted the frequency of the reference beam by 25 Hz using an acousto-optic modulator. The playback light focus is shown in Fig. 3(a). To verify the generation of higher harmonic modulated signals, we also shifted the frequency of the reference beam by 50 Hz (second harmonic) and 75 Hz (third harmonic) and measured the corresponding light fields. The playback light also forms foci through the scattering medium, but becomes weaker with higher harmonics [Fig. 3(b) and 3(c)]. As a control, we shifted the reference beam frequency by 30 Hz ( $\neq nf_m$ ) and no observable focus was made [Fig. 3(d)] due to the frequency mismatch between the tagged light and

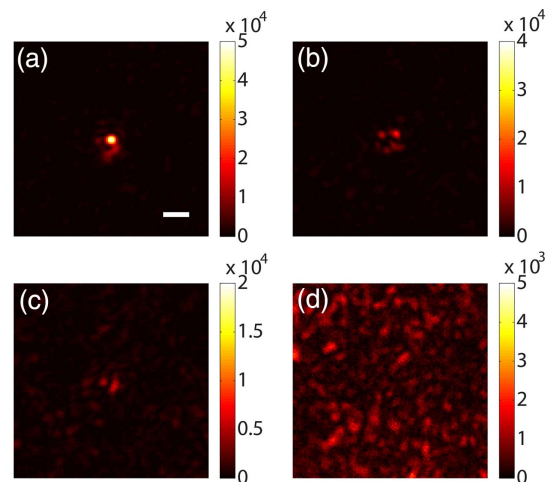


**Fig. 3.** Magnetic-particle-guided optical focusing with the frequency modulation method. The electromagnets were driven by 25 Hz rectangular waves. Images were captured with the setup shown in Fig. 2(b). The focus achieved when the reference beam frequency was shifted by (a) 25 Hz (fundamental frequency), (b) 50 Hz (second harmonic), and (c) 75 Hz (third harmonic) relative to the laser frequency. (d) Control experiment: no focus was observed when the reference beam frequency was shifted by 30 Hz (frequency mismatch). Scale bar, 5  $\mu\text{m}$ .

reference beam. Using the same method to quantify the focus created with the fundamental frequency, we found that the PBR of the focus in Fig. 3(a) is  $128 \pm 6$  with a focal spot size of  $1.44 \pm 0.08 \mu\text{m}$ .

### B. Focusing Light onto Magnetic-Particle-Tagged Cells inside Scattering Media

The magnetic particle guidestar can be used for optical targeting of cells of interest, for applications such as photothermal or photodynamic therapy. In this scenario, specific cells can be targeted by the magnetic particles through endocytosis or membrane attachment. Then, by performing magnetic-particle-guided focusing, we can find the correct wavefront solution to allow light to be focused to the desired cell, even when the cell is located deep inside scattering tissue.

As a first step toward this long-term goal, we demonstrated a proof-of-concept experiment based on macrophage cells because macrophages readily endocytose nanoparticles and are the primary cells in the body for the initial uptake of nanoparticles. We added the magnetic particles (453 nm mean diameter; see Fig. S3 of Supplement 1 for particle characterization) to the cells (see Supplement 1 for sample preparation and for cell viability measurement results shown in Fig. S4). After the cells engulfed the particles, the sample was loaded into a microfluidic channel. Figure 4(a) and 4(b) show bright-field images of a cell that endocytosed the magnetic particles as it was being driven by magnetic fields of two different directions. The observable displacement of  $2.2 \mu\text{m}$  shows great promise for focusing light using the field subtraction method. Based on this mechanism, we were able to focus light between two pieces of 1-mm-thick tissue (Fig. 4(c)). We also demonstrated optical focusing using the frequency modulation method, in which we used a 25 Hz AC magnetic field to oscillate the magnetic particles (Visualization 3 and Visualization 4). By measuring the frequency-shifted light, we were able to focus light to the cell with magnetic particles [Fig. 4(d)]. As a control, when we shifted the phase pattern displayed on the SLM by 10 pixels in both directions, we observed

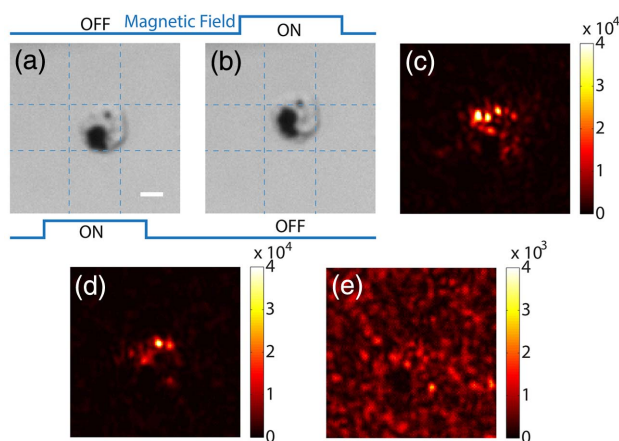


**Fig. 4.** Focusing light onto a targeted cell that endocytosed magnetic particles of 453 nm diameter. Panels (a) and (b) show bright-field images of a cell under two magnetic fields. (c) Focus achieved by the field subtraction method. (d) Focus achieved by the frequency modulation method ( $f_m = 25 \text{ Hz}$ ). (e) Control experiment: no focus was observed when the SLM pattern was circularly shifted by  $10 \times 10$  pixels after obtaining the result in (d). Scale bar,  $5 \mu\text{m}$ .

a background image without a discernable focus [Fig. 4(e)]. The PBRs of the foci achieved by the two methods were  $125 \pm 2$  and  $95 \pm 2$ , based on the aforementioned calculation method.

### C. Focusing Light to Different Target Locations inside Scattering Media

In contrast to conventional physical guidestars, which limit the optical focus to a fixed location, the magnetic guidestar can be moved to a target position by controlling the external magnetic field. As a proof-of-concept demonstration, we used a magnet to move the magnetic particles in 50% glycerol mixed with water through a microfluidic channel to a target location monitored through a wide-field microscope as shown in Fig. 2(b). We then sandwiched the sample between two pieces of 1-mm-thick chicken tissue [Fig. 2(a)] and implemented the frequency modulation method to focus light to the particles. The above process was repeated five times to form foci at five target locations along a line with a step size of  $30 \mu\text{m}$ . The image of the focus at each location is shown in Fig. 5.

## 4. DISCUSSION AND CONCLUSIONS

We developed and experimentally demonstrated a new guidestar mechanism for optical wavefront shaping, which uses a magnetic field to guide optical focusing inside scattering media. Although the ultrasound guidestar is truly noninvasive and is able to target arbitrary positions, it has limited penetration depths due to strong absorption of high-frequency ultrasound (e.g., 50 MHz). Unfortunately, the use of high frequencies for ultrasound guidestars is critical, not only because it provides higher resolution, but also because the small focal size reduces the number of optical modes inside the focus, which is inversely proportional to the intensity of the focus [44]. While low-frequency ultrasound (e.g., 1 MHz) with the microbubble guidestar can potentially address this issue, microbubbles are currently limited to the vasculature and are not stable for continuous focusing. Moreover, ultrasound of MHz-order frequencies is significantly attenuated by bone structures (e.g., skull) and gas bodies (e.g., pulmonary alveoli). In contrast, magnetic fields have full-body penetration and

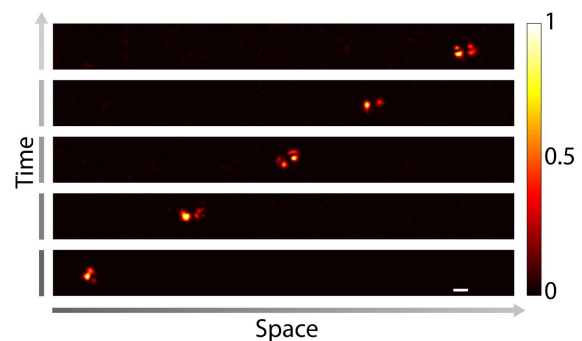


**Fig. 5.** Focusing light to different target locations by controlling the positions of the magnetic particles using an external magnetic field. The magnetic particles were driven to the target locations inside a microfluidic channel based on the position feedback from the observation microscope [Fig. 2(b)]. After reaching each target location, the magnetic particles were covered by the scattering samples on both sides as shown in Fig. 2(a), and the DOPC process was performed to create a focus through the scattering sample on the DOPC system side. Then, the scattering sample on the observation microscope side was removed [Fig. 2(b)], and the focus was observed directly. Scale bar,  $5 \mu\text{m}$ .

magnetic particles can be functionalized and can enter many locations beyond the vasculature. These features promise to benefit some important biomedical applications such as targeted therapy [45] or neural modulation [46] many millimeters deep in soft tissue and/or through the skull. The magnetic guidestar can also be implanted to a target location for light-based bioelectronics [47]. Interestingly, magnetic particles can be moved within soft tissue by manipulating the external magnetic field [48,49], significantly increasing the flexibility of this method. By combining this ability with a magnetic imaging modality such as MRI or magnetic particle imaging [50] to monitor the location of the particles as they are moved by an external field, the position of the magnetic-guidestar-assisted optical focus can be controlled, thus enabling deep-tissue optical imaging.

The magnetic guidestar has strong modulation efficiency, since the displacement of magnetic particles can be larger than the wavelength of light. In our experiments, we measured the magnetic-particle-tagged light using two wavefront measurement methods—the field subtraction method and the frequency modulation method. The latter method uses a lock-in scheme to measure the frequency-shifted light from the magnetic particles. While this narrow-band detection method effectively rejects wide-band noise, it also excludes the harmonic signals resulting from the particle oscillation. As a consequence, the modulation efficiency of the frequency modulation method (5%) is lower than that of the field subtraction method (29%) (see Fig. S5, Supplement 1), which measures any fluctuation between two measurements. In either case, the modulation efficiency is higher than that of the ultrasound guidestar (1%) [32]. When the magnetic particle is smaller than the size of an optical mode, the modulation efficiency is reduced. Although single nanoparticles are desirable in some applications, they commonly accumulate in endosomes into aggregates hundreds of nanometers in size [36], which is on the same scale as optical wavelengths.

Taking advantage of the high modulation efficiency and the small number of optical modes inside the optical focus, the magnetic guidestar enables a PBR of  $>100$ , an order of magnitude higher than that of the ultrasound guidestar. However, this PBR is still significantly lower than that calculated based on the ratio of the number of controlled optical modes ( $2.2 \times 10^5$ ) and the number of targeted modes [44] (8 for the  $2.5 \mu\text{m}$  magnetic particles and 22 for the cell; see Supplement 1, Experimental Setup, for a detailed calculation). This discrepancy is due in part to other magnetic particles outside the field of view of the observation camera, which lead to a larger number of optical modes being modulated than we observe. Moreover, the signal-to-noise ratio (SNR) of the measured field is also lower than in the direct DOPC case [51]. It should also be noted that the SNR of the measured field is additionally affected by the intensity of the optical speckle produced by the mutual interference of randomly scattered light on the magnetic particle during the experiment, since the size of the particle is on the same scale as the speckle grains.

To translate this technique into *in vivo* applications, we also need to improve the speed of the DOPC process. Currently, the wavefront measurement took 2 s (averaging 10 times) for the frequency modulation method and 400 ms for the field subtraction method, which is much longer than the speckle decorrelation time associated with living biological tissue (one millisecond to tens of milliseconds [11,13,14]). The low speed is largely due to the low frame rate of the camera (20 frames per second),

the data transfer rate, and the slow response of the SLM. Future work to improve the speed of the system includes using a higher power illumination source to reduce the camera exposure time and improving the DOPC system speed by using recently developed high-speed systems [52,53].

In summary, we demonstrated a magnetic-field-controlled guidestar for focusing light deep inside scattering media using optical phase conjugation. Compared with the optical and ultrasonic fields, the magnetic field has an exceptional penetration depth. The magnetic particle guidestar has a high light-tagging efficiency, good biocompatibility, and a small diameter, which enables sharp and bright focusing deep inside biological tissue. This new method can potentially benefit a wide range of biomedical applications, including deep-tissue imaging, neural modulation, and targeted photothermal and photodynamic therapies.

**Funding.** National Institutes of Health (NIH) (F31EB021153, U01NS090577); GIST-Caltech Collaborative Research Proposal (CG2016); Donna and Benjamin M. Rosen Bioengineering Center; Israel-City of Hope Fellowship Program in Biomedical Research.

**Acknowledgment.** The authors would like to thank Dr. Euiheon Chung, Dr. Mooseok Jang, Dr. Ethan White, Dr. Kathleen Elison, Dr. Mikhail Shapiro, Dr. George Lu, and Mr. Hunter Davis for assistance and helpful discussions. TEM imaging was conducted at the Electron Microscopy core at City of Hope with Marcia Millier, Zhuo Li and Ricardo Zerda.

See Supplement 1 for supporting content.

## REFERENCES

1. V. Ntziachristos, "Going deeper than microscopy: the optical imaging frontier in biology," *Nat. Methods* **7**, 603–614 (2010).
2. I. M. Vellekoop and A. P. Mosk, "Focusing coherent light through opaque strongly scattering media," *Opt. Lett.* **32**, 2309–2311 (2007).
3. I. M. Vellekoop, "Feedback-based wavefront shaping," *Opt. Express* **23**, 12189–12206 (2015).
4. A. P. Mosk, A. Lagendijk, G. Lerosey, and M. Fink, "Controlling waves in space and time for imaging and focusing in complex media," *Nat. Photonics* **6**, 283–292 (2012).
5. R. Horstmeyer, H. Ruan, and C. Yang, "Guidestar-assisted wavefront-shaping methods for focusing light into biological tissue," *Nat. Photonics* **9**, 563–571 (2015).
6. H. Yu, J. Park, K. Lee, J. Yoon, K. Kim, S. Lee, and Y. Park, "Recent advances in wavefront shaping techniques for biomedical applications," *Curr. Appl. Phys.* **15**, 632–641 (2015).
7. S. M. Popoff, G. Lerosey, R. Carminati, M. Fink, A. C. Boccara, and S. Gigan, "Measuring the transmission matrix in optics: an approach to the study and control of light propagation in disordered media," *Phys. Rev. Lett.* **104**, 100601 (2010).
8. M. Kim, W. Choi, Y. Choi, C. Yoon, and W. Choi, "Transmission matrix of a scattering medium and its applications in biophotonics," *Opt. Express* **23**, 12648–12668 (2015).
9. T. Chaigne, O. Katz, A. C. Boccara, M. Fink, E. Bossy, and S. Gigan, "Controlling light in scattering media non-invasively using the photo-acoustic transmission matrix," *Nat. Photonics* **8**, 58–64 (2013).
10. H. Yu, T. R. Hillman, W. Choi, J. O. Lee, M. S. Feld, R. R. Dasari, and Y. Park, "Measuring large optical transmission matrices of disordered media," *Phys. Rev. Lett.* **111**, 153902 (2013).
11. M. Jang, H. Ruan, I. M. Vellekoop, B. Judkewitz, E. Chung, and C. Yang, "Relation between speckle decorrelation and optical phase conjugation (OPC)-based turbidity suppression through dynamic scattering media: a study on *in vivo* mouse skin," *Biomed. Opt. Express* **6**, 72–85 (2015).

12. J. Brake, M. Jang, and C. Yang, "Analyzing the relationship between decorrelation time and tissue thickness in acute rat brain slices using multispeckle diffusing wave spectroscopy," *J. Opt. Soc. Am. A* **33**, 270–275 (2016).
13. Y. Liu, P. Lai, C. Ma, X. Xu, A. A. Grabar, and L. V. Wang, "Optical focusing deep inside dynamic scattering media with near-infrared time-reversed ultrasonically encoded (TRUE) light," *Nat. Commun.* **6**, 5904 (2015).
14. M. M. Qureshi, J. Brake, H.-J. Jeon, H. Ruan, Y. Liu, A. M. Safi, T. J. Eom, C. Yang, and E. Chung, "In vivo study of optical speckle decorrelation time across depths in the mouse brain," *Biomed. Opt. Express* **8**, 4855–4864 (2017).
15. M. Cui and C. Yang, "Implementation of a digital optical phase conjugation system and its application to study the robustness of turbidity suppression by phase conjugation," *Opt. Express* **18**, 3444–3455 (2010).
16. C. Hsieh, Y. Pu, R. Grange, and D. Psaltis, "Digital phase conjugation of second harmonic radiation emitted by nanoparticles in turbid media," *Opt. Express* **18**, 12283–12290 (2010).
17. I. N. Papadopoulos, S. Farahi, C. Moser, and D. Psaltis, "Focusing and scanning light through a multimode optical fiber using digital phase conjugation," *Opt. Express* **20**, 10583–10590 (2012).
18. T. R. Hillman, T. Yamauchi, W. Choi, R. R. Dasari, M. S. Feld, Y. Park, and Z. Yaqoob, "Digital optical phase conjugation for delivering two-dimensional images through turbid media," *Sci. Rep.* **3**, 1909 (2013).
19. K. Lee, J. Lee, J.-H. Park, J.-H. Park, and Y. Park, "One-wave optical phase conjugation mirror by actively coupling arbitrary light fields into a single-mode reflector," *Phys. Rev. Lett.* **115**, 153902 (2015).
20. Y. Shen, Y. Liu, C. Ma, and L. V. Wang, "Focusing light through biological tissue and tissue-mimicking phantoms up to 9.6 cm in thickness with digital optical phase conjugation," *J. Biomed. Opt.* **21**, 085001 (2016).
21. N. Ji, D. E. Milkie, and E. Betzig, "Adaptive optics via pupil segmentation for high-resolution imaging in biological tissues," *Nat. Methods* **7**, 141–147 (2010).
22. I. M. Vellekoop and C. M. Aegerter, "Scattered light fluorescence microscopy: imaging through turbid layers," *Opt. Lett.* **35**, 1245–1247 (2010).
23. F. Kong, R. H. Silverman, L. Liu, P. V. Chitnis, K. K. Lee, and Y. C. Chen, "Photoacoustic-guided convergence of light through optically diffusive media," *Opt. Lett.* **36**, 2053–2055 (2011).
24. O. Tzang, E. Niv, A. M. Caravaca-Aguirre, and R. Piestun, "Thermal expansion feedback for wave-front shaping," *Opt. Express* **25**, 6122–6131 (2017).
25. P. Lai, L. Wang, J. W. Tay, and L. V. Wang, "Photoacoustically guided wavefront shaping for enhanced optical focusing in scattering media," *Nat. Photonics* **9**, 126–132 (2015).
26. J. Jang, J. Lim, H. Yu, H. Choi, J. Ha, J.-H. Park, W.-Y. Oh, W. Jang, S. Lee, and Y. Park, "Complex wavefront shaping for optimal depth-selective focusing in optical coherence tomography," *Opt. Express* **21**, 2890–2902 (2013).
27. X. Xu, H. Liu, and L. V. Wang, "Time-reversed ultrasonically encoded optical focusing into scattering media," *Nat. Photonics* **5**, 154–157 (2011).
28. Y. M. Wang, B. Judkewitz, C. A. DiMarzio, and C. Yang, "Deep-tissue focal fluorescence imaging with digitally time-reversed ultrasound-encoded light," *Nat. Commun.* **3**, 928 (2012).
29. K. Si, R. Fiolka, and M. Cui, "Fluorescence imaging beyond the ballistic regime by ultrasound pulse guided digital phase conjugation," *Nat. Photonics* **6**, 657–661 (2012).
30. H. Ruan, M. Jang, B. Judkewitz, and C. Yang, "Iterative time-reversed ultrasonically encoded light focusing in backscattering mode," *Sci. Rep.* **4**, 7156 (2014).
31. J. W. Tay, P. Lai, Y. Suzuki, and L. V. Wang, "Ultrasonically encoded wavefront shaping for focusing into random media," *Sci. Rep.* **4**, 3918 (2014).
32. H. Ruan, M. Jang, and C. Yang, "Optical focusing inside scattering media with time-reversed ultrasound microbubble encoded light," *Nat. Commun.* **6**, 8968 (2015).
33. C. Ma, X. Xu, Y. Liu, and L. V. Wang, "Time-reversed adapted-perturbation (TRAP) optical focusing onto dynamic objects inside scattering media," *Nat. Photonics* **8**, 931–936 (2014).
34. E. H. Zhou, H. Ruan, C. Yang, and B. Judkewitz, "Focusing on moving targets through scattering samples," *Optica* **1**, 227–232 (2014).
35. B. D. Plouffe, S. K. Murthy, and L. H. Lewis, "Fundamentals and application of magnetic particles in cell isolation and enrichment: a review," *Rep. Prog. Phys.* **78**, 016601 (2015).
36. E. E. White, A. Pai, Y. Weng, A. K. Suresh, D. Van Haute, T. Pailevanian, D. Alizadeh, A. Hajimiri, B. Badie, and J. M. Berlin, "Functionalized iron oxide nanoparticles for controlling the movement of immune cells," *Nanoscale* **7**, 7780–7789 (2015).
37. C. S. S. R. Kumar and F. Mohammad, "Magnetic nanomaterials for hyperthermia-based therapy and controlled drug delivery," *Adv. Drug Deliv. Rev.* **63**, 789–808 (2011).
38. R. Chen, G. Romero, M. G. Christiansen, A. Mohr, and P. Anikeeva, "Wireless magnetothermal deep brain stimulation," *Science* **347**, 1477–1480 (2015).
39. E. N. Leith and J. Upatnieks, "Holographic imagery through diffusing media," *J. Opt. Soc. Am.* **56**, 523 (1966).
40. Z. Yaqoob, D. Psaltis, M. S. Feld, and C. Yang, "Optical phase conjugation for turbidity suppression in biological samples," *Nat. Photonics* **2**, 110–115 (2008).
41. I. Yamaguchi and T. Zhang, "Phase-shifting digital holography," *Opt. Lett.* **22**, 1268–1270 (1997).
42. A. Schlegel, S. F. Alvarado, and P. Wachter, "Optical properties of magnetite (Fe<sub>3</sub>O<sub>4</sub>) related content optical properties of magnetite (Fe, O)," *J. Phys. C* **12**, 1157–1164 (1979).
43. H. Ruan, M. L. Mather, and S. P. Morgan, "Pulsed ultrasound modulated optical tomography with harmonic lock-in holography detection," *J. Opt. Soc. Am. A* **30**, 1409–1416 (2013).
44. I. M. Vellekoop, E. G. van Putten, A. Lagendijk, and A. P. Mosk, "Demixing light paths inside disordered metamaterials," *Opt. Express* **16**, 67–80 (2008).
45. R. Mooney, L. Roma, D. Zhao, D. Van Haute, E. Garcia, S. U. Kim, A. J. Annala, K. S. Aboody, and J. M. Berlin, "Neural stem cell-mediated intratumoral delivery of gold nanorods improves photothermal therapy," *ACS Nano* **8**, 12450–12460 (2014).
46. H. Ruan, J. Brake, J. E. Robinson, M. Jang, C. Xiao, C. Zhou, V. Gradinaru, and C. Yang, "Optogenetic control of neural activity with time-reversed ultrasound encoded light," in *Optics in the Life Sciences Congress (OSA, 2017)*, p. BrM3B.3.
47. K. Birmingham, V. Gradinaru, P. Anikeeva, W. M. Grill, V. Píkov, B. McLaughlin, P. Pasricha, D. Weber, K. Ludwig, and K. Famm, "Bioelectronic medicines: a research roadmap," *Nat. Rev. Drug Discov.* **13**, 399–400 (2014).
48. S. Kulkarni, B. Ramaswamy, E. Horton, S. Gangapuram, A. Nacev, D. Depireux, M. Shimoji, and B. Shapiro, "Quantifying the motion of magnetic particles in excised tissue: effect of particle properties and applied magnetic field," *J. Magn. Magn. Mater.* **393**, 243–252 (2015).
49. R. Guduru, P. Liang, J. Hong, A. Rodzinski, A. Hadjikhani, J. Horstmyer, E. Levister, and S. Khizroev, "Magnetolectric "spin" on stimulating the brain," *Nanomedicine* **10**, 2051–2061 (2015).
50. B. Gleich and J. Weizenecker, "Tomographic imaging using the nonlinear response of magnetic particles," *Nature* **435**, 1214–1217 (2005).
51. M. Jang, H. Ruan, H. Zhou, B. Judkewitz, and C. Yang, "Method for auto-alignment of digital optical phase conjugation systems based on digital propagation," *Opt. Express* **22**, 14054–14071 (2014).
52. D. Wang, E. H. Zhou, J. Brake, H. Ruan, M. Jang, and C. Yang, "Focusing through dynamic tissue with millisecond digital optical phase conjugation," *Optica* **2**, 728–735 (2015).
53. Y. Liu, C. Ma, Y. Shen, J. Shi, and L. V. Wang, "Focusing light inside dynamic scattering media with millisecond digital optical phase conjugation," *Optica* **4**, 280–288 (2017).